Title: Photonic Axion Insulator

Authors: Gui-Geng Liu[1,2]†, Subhaskar Mandal[1]†, Xiang Xi[3]†, Qiang Wang[4]†, Chiara Devescovi[5,6], Antonio Morales-Pérez[5,7], Ziyao Wang[8], Linyun Yang[8], Rimi Banerjee[1], Yang Long[1], Yan Meng[3], Peiheng Zhou[9], Zhen Gao[8,10], Yidong Chong[1,11], Aitzol García-Etxarri[5,12], Maia G. Vergniory[5,13,14], Baile Zhang[1,11]*

Affiliations:

[1]Division of Physics and Applied Physics, School of Physical and Mathematical Sciences, Nanyang Technological University; Singapore, 637371, Singapore.

[2]Research Center for Industries of the Future, School of Engineering, Westlake University; Hangzhou, 310030, China.

[3]School of Electrical Engineering and Intelligentization, Dongguan University of Technology; Dongguan, 523000, China.

[4]National Laboratory of Solid State Microstructures and School of Physics, Collaborative Innovation Center of Advanced Microstructures, Nanjing University; Nanjing, 210093, China.

[5]Donostia International Physics Center; Donostia-San Sebastian, 20018, Spain.

[6]Institute for Theoretical Physics, ETH Zurich; Zurich, 8093, Switzerland.

[7]Material and Applied Physics Department, University of the Basque Country (UPV/EHU); Donostia-San Sebastián, 20080, Spain.

[8]Department of Electronic and Electrical Engineering, Southern University of Science and Technology; Shenzhen, 518055, China.

[9]National Engineering Research Center of Electromagnetic Radiation Control Materials, Key Laboratory of Multi-spectral Absorbing Materials and Structures of Ministry of Education, University of Electronic Science and Technology of China; Chengdu, 610054, China.

[10]State Key Laboratory of Optical Fiber and Cable Manufacture Technology, Department of Electronic and Electrical Engineering, Guangdong Key Laboratory of Integrated Optoelectronics Intellisense, Southern University of Science and Technology; Shenzhen 518055, China.

[11]Centre for Disruptive Photonic Technologies, The Photonics Institute, Nanyang Technological University; Singapore, 637371, Singapore.

[12]IKERBASQUE, Basque Foundation for Science; Bilbao, 48011, Spain.

[13]Max Planck Institute for Chemical Physics of Solids; Dresden, 01187, Germany.

[14]Département de Physique et Institut Quantique, Université de Sherbrooke; Sherbrooke, J1K 2R1, Canada.

†These authors contributed equally to this work.

37 *Corresponding author. Email: blzhang@ntu.edu.sg

Abstract: Axions, hypothetical elementary particles still undetectable in nature, can arise as quasiparticles in three-dimensional crystals known as axion insulators. Previous implementations of axion insulators have been largely limited to two-dimensional systems, leaving their topological properties in three dimensions unexplored in experiment. Here, we realize an axion insulator in a three-dimensional photonic crystal and probe its topological properties. Demonstrated unique features include half-quantized Chern numbers on each surface that resembles a fractional Chern insulator, unidirectional chiral hinge states forming topological transport in three dimensions, and arithmetic operations between fractional and integer Chern numbers. Our work experimentally establishes the axion insulator as a three-dimensional topological phase of matter, and enables chiral states to form complex, unidirectional three-dimensional networks through braiding.

Main Text: The hypothetical axionic particles, originally proposed to solve the strong charge-parity (CP) problem in the Standard Model and later predicted to constitute dark matter, still remain elusive from detection in nature (*1-7*). However, it is now understood that axions can emerge as collective excitations, or quasiparticles, in certain crystals known as axion insulators (AXIs) (*8*). Like their elementary counterparts, these quasiparticles are governed by an axion field, which introduces an additional term $\theta\mathbf{E}\cdot\mathbf{B}$ (where θ is the axion angle defined modulo 2π and **E**, **B** are the electric and magnetic fields, respectively) into the electromagnetic Lagrangian, leading to "axion electrodynamics" with modified Maxwell's equations (*9*). In the crystal environment, the axion field can be quantized to act as a topological invariant that characterizes three-dimensional (3D) band topology, suggesting AXIs as a strong 3D topological phase of matter (*10*).

First we compare a 3D axion insulator with the paradigmatic two-dimensional (2D) Chern insulator that is well-known for its integer quantization (*11*, *12*). The 2D Chern insulator (Fig. 1A) is characterized by a bulk integer Chern number ($C = -1$ in the illustration), which dictates the number of chiral states propagating unidirectionally around the edges.

The 3D AXI (Fig. 1, B and C), on the other hand, is characterized by a quantized axion angle $\theta = \pi$ in the bulk, which induces a half-quantized Chern number C_s=±1/2 on all surfaces (*13*, *14*). Each surface thus behaves as a fractional Chern insulator (*15*–*23*) (recently discovered lattice analogues of the fractional quantum Hall effect), but not relying on strong inter-particle correlations. The half-quantization gives rise to the following physical signatures. Firstly, along each hinge between two adjacent surfaces with opposite half-quantized Chern numbers C_s=±1/2, an integer (unit) number of chiral states arise (Fig. 1B), giving rise to topological chiral transport in 3D space. Secondly, if a 2D Chern insulator with an integer Chern number C= –1 is attached to the top surface of the 3D AXI, the half-quantized Chern number will be changed from C_s=+1/2 to C_s=–1/2 (Fig. 1C), thus redirecting the flow of chiral states (*24*).

An ideal AXI shows potential for achieving topological transport in 3D (*13*, *14*, *24*) and enabling physical operations between integer and fractional Chern numbers (Fig. 1, B and C). However, previously AXIs were predominantly implemented either on a 2D interface (*25*–*29*), such as between a 3D topological insulator and a ferromagnet, or in quasi-2D thin film geometries of intrinsic magnetic materials such as $MnBi_2Te_4$ (*30*–*32*).

We report the experimental realization of an AXI in a 3D photonic crystal. The crystal comprises a 3D stack of 2D photonic Chern insulators (photonic crystal implementations of Chern insulators (*33*)) with alternating Chern numbers of ±1 (*34*) (Fig. 2A). With mirror-reflection

symmetry along *z*-axis, the crystal behaves as a photonic antiferromagnetic topological insulator (*34*), with side surfaces exhibiting a single surface Dirac cone—a long-sought feature for 3D photonic topological insulators (*35*). When the mirror-reflection symmetry along *z*-axis is broken (*36*), the crystal becomes an ideal AXI (*14*), characterized by a bulk axion angle $\theta = \pi$ and gapped surfaces possessing surface Chern numbers of C_s=±1/2. Through near-field microwave measurements, we map the chiral hinge states between adjacent surfaces with opposite surface Chern numbers, thus obtaining direct evidence for the "surface Chern insulator" behaviour (*36*). We also demonstrate the redirection of the flow of chiral states due to the change in the surface Chern number from +1/2 to −1/2 by adding a layer with C=−1 from another photonic Chern insulator, confirming the interplay between fractional and integer Chern numbers. Further substantiating topological transport in 3D, we demonstrate the intricate braiding of chiral states to form a variety of 3D unidirectional networks, including knots and links, which cannot be projected to 2D.

Photonic single surface Dirac cone

To construct the antiferromagnetic stacking (Fig. 2A), we consider the tight-binding model (Fig. 2B) consisting of stacked 2D Haldane model layers with alternating magnetic flux directions (i.e., alternating Chern numbers of ±1), with adjacent layers coupled through alternating interlayer hoppings t_{z1} and t_{z2} (see supplementary text for more details of the tight-binding model (*37*)). Initially, we set $t_{z1} = t_{z2}$ to preserve the mirror-reflection symmetry along the *z*-axis. This symmetry produces a nontrivial mirror Chern number that protects a single surface Dirac cone on the zigzag side surfaces in a finite sample (*38*), while the top and bottom surfaces remain gapped (see supplementary text and fig. S1 for more detailed calculations (*37*)).

The 3D tight binding model can be implemented in a 3D photonic crystal (Fig. 2C), in which the designed unit cell of the photonic crystal is composed of two gyromagnetic rods, sandwiched between and biased by two pairs of permanent magnets alongside two metallic plates perforated with holes. Triangular holes located at two sets of inequivalent corners of the hexagonal unit cell are perforated onto the metallic plates with side lengths of b_1 and b_2 to enable interlayer coupling. By ensuring $b_1 = b_2$, mirror-reflection symmetry is maintained along the *z*-axis. These adjacent gyromagnetic rods are magnetically biased in opposite directions to achieve the antiferromagnetic configuration (*30*), which gaps the 3D Dirac point in the photonic crystal and opens a complete bulk bandgap from 11.19 to 12.58 GHz (see fig. S5 for details (*37*)). Surface states in the zigzag side surfaces exhibit a single Dirac cone, protected by the nontrivial mirror Chern number (see supplementary text and figs. S6 to S8 for the topological invariant calculation and band simulation (*37*)). Such a photonic single surface Dirac cone has been long sought after for 3D photonic topological insulators (*35*).

Following this design, we construct the experimental sample shown in Fig. 2, D to F. To probe the surface states, the A1 surface of the photonic crystal (parallel to the *x*-*z* plane; see Fig. 2G) is covered with copper cladding to prevent wave leakage into the surrounding environment, while the other surfaces are wrapped with microwave absorbers. A point source is placed near the center of the A1 surface to excite surface states. The field distributions are mapped using a near-field scanning probe (see supplementary text (*37*)) and then Fourier-transformed to obtain the surface dispersion contour. The measured surface states form a single Dirac cone near 11.66 GHz

(Fig. 2H), which is in excellent agreement with theoretical predictions and simulations (see fig. S1B and fig. S6A).

Design of photonic Axion insulator

We then break the mirror-reflection symmetry along the *z*-axis by setting $t_{z1} \neq t_{z2}$ in the tight-binding model. In the photonic crystal design, this can be achieved by adjusting the hole sizes to make $b_1 \neq b_2$, for example, b_1 = 10 mm, b_2 = 5 mm (Fig. 3A). In this scenario, the photonic crystal becomes an AXI, with: (1) its bulk characterized by the axion angle $\theta = \pi$, (2) all surfaces being gapped and possessing a half surface Chern number of $C_s = \pm 1/2$, and (3) chiral hinge states spanning 11.53 GHz to 12.35 GHz (see supplementary text and figs. S2 to S6 for more details with tight binding analysis and numerical simulations (*37*)). Intuitively, the half-quantized surface Chern number on the side surfaces can be understood to arise from gapping the single surface Dirac cone, similar to the previous surface gapping in 3D topological insulators (*25–29*, *39*, *40*). The half surface Chern number on the top and bottom surfaces requires further analysis, which can be found in fig. S4, fig. S6 and fig. S8.

Measurements of chiral hinge states

To measure the chiral hinge states (see fig. S10 for the fabricated sample (*37*)), we cover the two surfaces adjacent to the hinge H1 (Fig. 3B) with copper claddings while the other surfaces are wrapped with microwave absorbers. By placing a point source near the hinge H1 and scanning the excited fields throughout the sample, we find that the fields at 11.9 GHz only propagate along the +*z* direction near the hinge H1, and with almost no fields observed propagating backward (Fig. 3B). Additionally, even with a large copper plate inserted as a metallic obstacle, the hinge states are observed to bypass the obstacle and continue their propagation without any backscattering (Fig. 3C), thus confirming the unidirectional propagation of the chiral hinge states and their robustness against obstructions.

We also measure the frequency-dependent transmission spectra of hinge states by positioning two source antennas at two ends of hinge H1, respectively (Fig. 3D). For the backward transmission (red line in Fig. 3D), a dip is observed around 11.6-12.2 GHz, manifesting a complete gap of the surface and bulk states. However, the forward transmission (blue solid line in Fig. 3D) shows a strong signal, approximately 40 dB greater than the backward transmission at mid-gap frequencies. Even with a large obstacle on the hinge (for the case in Fig. 3C), the forward transmission (blue dashed line in Fig. 3D) maintains a level approximately 30 dB greater than the backward transmission within the gap. Furthermore, by performing a Fourier transform of the measured fields near hinge H1, we obtain the dispersion of the hinge states, displaying positive group velocities along the k_z direction, indicative of chiral propagation (Fig. 3E, see more details and results in fig. S9).

Arithmetic operation between fractional and integer Chern numbers

To map out the closed trajectories of the chiral hinge states, we first consider a sample with a parallelogram-like prism structure containing an odd number of photonic Chern insulator layers (Fig. 3F). At hinges H1 and H2, the hinge states propagate in the +*z* and −*z* directions, respectively.

The top and bottom surfaces have surface Chern numbers of +1/2 and −1/2 (indicated in yellow and blue for all surfaces in Fig. 3F), respectively. The hinge states propagate anticlockwise within both the top and bottom surfaces, forming a closed loop. To observe this experimentally, we cover all surfaces of the sample with copper claddings, and scan the fields excited by two point sources (see supplementary text for experimental details (*37*)). The measured results (Fig. 3G), show a closed loop, in agreement with the predictions. We note that other 3D topological phases can also host chiral hinge states, though not on all hinges (*41*).

We then attach one more photonic Chern insulator layer with Chern number −1 to the top surface of the 3D AXI (Fig. 3H). This causes the surface Chern number on the top surface to change from +1/2 to −1/2, and thus the propagation direction of chiral hinge states in the top surface become clockwise. The resulting closed-loop configuration of the chiral hinge states (Fig. 3H) is verified through experimental mapping (Fig. 3I).

We also construct a hexagonal prism-shaped sample with an odd number of photonic Chern insulator layers (Fig. 3J). A closed loop traversing all vertical hinges is formed (Fig. 3, J and K). By adjusting the sample to be even number of layers, both the top and bottom surfaces have the surface Chern number −1/2, generating three isolated loops at the side surfaces (Fig. 3L), which is further experimentally confirmed (Fig. 3M). Hence, each of those three side surfaces acts as a conventional 2D Chern insulator (*11*, *12*).

Braiding of chiral hinge states

As a final demonstration of the distinctive topological transport features of the AXI, we implement samples where the chiral hinge states are braided into complex knots and links in 3D space. Figure 4, A and B, depict a photonic crystal where chiral hinge states exhibit a trefoil knot in 3D space (the topology is illustrated in Fig. 4C). Copper plates are integrated into the crystal to facilitate the self-braiding of chiral hinge states. The detailed construction is illustrated in fig. S11, A to H. We also engineer a composite structure by merging two parallelogram-shaped prisms (Fig. 4D), creating a Hopf link (Fig. 4E) (the topology is illustrated in Fig. 4F). For more details of the design and the analysis, see fig. S11, I to N.

Outlook

The above results clearly demonstrate the realization of an AXI in a 3D photonic crystal. The interaction between fractional and integer Chern numbers opens new avenues in topological physics, offering insights that could guide similar demonstrations in condensed matter or cold atom systems. While demonstrating fixed values of quantized axion field angle $\theta = \pi$ and half Chern numbers of $\pm 1/2$, other values could potentially be achieved through the engineering of spins for axion quasiparticles (*42*). Furthermore, the current setup may evolve to exhibit Majorana-like chiral hinge states (*43*), whose braiding may be valuable for topological quantum computing (*44*). Although implemented at microwave frequencies, other photonic realizations may also be possible at higher frequencies, given the successful realization of several 2D photonic Chern insulators at optical frequencies (*45*–*47*). Notably, current axion haloscopes seek to detect axions by converting them into detectable microwave photons under a strong magnetic field (*4*–*7*, *9*). Our photonic AXI could serve as a tabletop platform to investigate axion-photon interactions and other fundamental aspects of axion electrodynamics (*8*, *48*).

References

1. R. D. Peccei, H. R. Quinn, CP conservation in the presence of pseudoparticles. *Phys. Rev. Lett.* **38**, 1440–1443 (1977).
2. J. E. Kim, G. Carosi, Axions and the strong cp problem. *Rev. Mod. Phys.* **82**, 557 (2010).
3. J. Preskill, M. B. Wise, F. Wilczek, Cosmology of the invisible axion. *Phys. Rev. B* **120**, 127 (1983).
4. D. J. Marsh, Axion cosmology. *Phys. Rep.* **643**, 1-79 (2016).
5. E. Braaten, H. Zhang, Colloquium: The physics of axion stars. *Rev. Mod. Phys.* **91**, 041002 (2019).
6. F. Chadha-Day, J. Ellis, D. J. E. Marsh, Axion dark matter: What is it and why now? *Sci. Adv.* **8**, eabj3618 (2022).
7. Y. K. Semertzidis, S. Youn, Axion dark matter: How to see it? *Sci. Adv.* **8**, eabm9928 (2022).
8. F. Wilczek, Two applications of axion electrodynamics. *Phys. Rev. Lett.* **58**, 1799–1802 (1987).
9. P. Sikivie, Experimental tests of the "invisible" axion. *Phys. Rev. Lett.* **51**, 1415 (1983).
10. D. M. Nenno, C. A. C. Garcia, J. Gooth, C. Felser, P. Narang, Axion physics in condensed-matter systems. *Nat. Rev. Phys.* **2**, 682-696 (2020).
11. M. Z. Hasan, C. L. Kane, Colloquium: Topological insulators. *Rev. Mod. Phys.* **82**, 3045 (2010).
12. X.-L. Qi, S.-C. Zhang, Topological insulators and superconductors. *Rev. Mod. Phys.* **83**, 1057-1110 (2011).
13. N. Varnava, D. Vanderbilt, Surfaces of axion insulators. *Phys. Rev. B* **98**, 245117 (2018).
14. Y. Xu et al., High-throughput calculations of magnetic topological materials. *Nature* **586**, 702–707 (2020).
15. E. M. Spanton et al., Observation of fractional chern insulators in a van der waals heterostructure. *Science* **360**, 62-66 (2018).
16. Y. Xie et al., Fractional Chern insulators in magic-angle twisted bilayer graphene. *Nature* **600**, 439-443 (2021).
17. J. Cai et al., Signatures of fractional quantum anomalous Hall states in twisted MoTe2. *Nature* **622**, 63-68 (2023).
18. H. Park et al., Observation of fractionally quantized anomalous Hall effect. *Nature* **622**, 74-79 (2023).
19. Y. Zeng et al., Thermodynamic evidence of fractional Chern insulator in moiré MoTe2. *Nature* **622**, 69-73 (2023).
20. F. Xu et al.,Observation of integer and fractional quantum anomalous hall effects in twisted bilayer mote2. *Phys. Rev. X* **13**, 031037 (2023).
21. J. Léonard et al., Realization of a fractional quantum Hall state with ultracold atoms. *Nature* **619**, 495-499 (2023).
22. Z. Lu et al., Fractional quantum anomalous Hall effect in multilayer graphene. *Nature* **626**, 759-764 (2024).
23. C. Wang et al., Realization of fractional quantum hall state with interacting photons. *Science* **384**, 579-584 (2024).
24. B. J. Wieder, B. A. Bernevig, The axion insulator as a pump of fragile topology. arXiv:1810.02373 [cond-mat.mes-hall] (2018).
25. L. Wu et al., Quantized faraday and kerr rotation and axion electrodynamics of a 3d topological insulator. *Science* **354**, 1124-1127 (2016).
26. M. Mogi et al., Tailoring tricolor structure of magnetic topological insulator for robust axion

insulator. *Sci. Adv.* **3**, eaao1669 (2017).
27. M. Mogi et al., A magnetic heterostructure of topological insulators as a candidate for an axion insulator. *Nat. Mater.* **16**, 516–521 (2017).
28. D. Xiao et al., Realization of the axion insulator state in quantum anomalous hall sandwich heterostructures. *Phys. Rev. Lett.* **120**, 056801 (2018).
29. D. Zhuo et al., Axion insulator state in hundred-nanometer-thick magnetic topological insulator sandwich heterostructures. *Nat. Commun.* **14**, 7596 (2023).
30. M. M. Otrokov et al., Prediction and observation of an antiferromagnetic topological insulator. *Nature* **576**, 416–422 (2019).
31. C. Liu et al., Robust axion insulator and Chern insulator phases in a two-dimensional antiferromagnetic topological insulator. *Nat. Mater.* **19**, 522-527 (2020).
32. A. Gao et al., Layer Hall effect in a 2D topological axion antiferromagnet. *Nature* **595**, 521-525 (2021).
33. Z. Wang, Y. Chong, J. D. Joannopoulos, M. Soljačić, Observation of unidirectional backscattering-immune topological electromagnetic states. *Nature* **461**, 772-775 (2009).
34. I. C. Fulga, N. Avraham, H. Beidenkopf, A. Stern, Coupled-layer description of topological crystalline insulators. *Phys. Rev. B* **94**, 125405 (2016).
35. L. Lu et al., Symmetry-protected topological photonic crystal in three dimensions. *Nature Physics* **12**, 337-340 (2016).
36. C. Yue et al., Symmetry-enforced chiral hinge states and surface quantum anomalous Hall effect in the magnetic axion insulator Bi2–xSmxSe3. *Nat. Phys.* **15**, 577-581 (2019).
37. Materials, methods, and additional information are available as supplementary materials.
38. F. Schindler et al., Higher-order topological insulators. *Sci. Adv.* **4**, eaat0346 (2018).
39. R. Lu et al., Half-magnetic topological insulator with magnetization-induced dirac gap at a selected surface. *Phys. Rev. X* **11**, 011039 (2021).
40. M. Mogi et al., Experimental signature of the parity anomaly in a semi-magnetic topological insulator. *Nat. Phys.* **18**, 390-394 (2022).
41. X. Ni, Z. Xiao, A. B. Khanikaev, A. Alù, Robust multiplexing with topolectrical higher-order chern insulators. *Phys. Rev. Appl.* **13**, 064031 (2020).
42. S. Li, M. Gong, Y.-H. Li, H. Jiang, X. C. Xie, High spin axion insulator. *Nat. Commun.* **15**, 4250 (2024).
43. Q. Yan, H. Li, J. Zeng, Q.-F. Sun, X. C. Xie, A Majorana perspective on understanding and identifying axion insulators. *Commun. Phys.* **4**, 239 (2021).
44. C. Nayak, S. H. Simon, A. Stern, M. Freedman, S. Das Sarma, Non-abelian anyons and topological quantum computation. *Rev. Mod. Phys.* **80**, 1083-1159 (2008).
45. B. Bahari et al., Nonreciprocal lasing in topological cavities of arbitrary geometries. *Science* **358**, 636-640 (2017).
46. Y. G. N. Liu, P. S. Jung, M. Parto, D. N. Christodoulides, M. Khajavikhan, Gain-induced topological response via tailored long-range interactions. *Nat. Phys.* **17**, 704-709 (2021).
47. J. Jin et al., Observation of floquet chern insulators of light. arXiv:2304.09385 [physics.optics] (2023).
48. C. Devescovi et al., Axion topology in photonic crystal domain walls. *Nat. Commun.* **15**, 6814 (2024).
49. G.-G. Liu et al., Data for 3D Photonic Crystal, DR-NTU (Data) (2024); https://doi.org/10.21979/N9/XSPEHE.
50. A. Morales-Pérez et al., Transversality-enforced tight-binding model for 3d photonic crystals

aided by topological quantum chemistry. arXiv:2305.18257 [physics.optics] (2023).
51. F. D. M. Haldane, Model for a quantum hall effect without landau levels: Condensed-matter realization of the "parity anomaly". *Phys. Rev. Lett.* **61**, 2015 (1988).
52. G.-G. Liu et al., Topological Chern vectors in three-dimensional photonic crystals. *Nature* **609**, 925-930 (2022).
53. W. A. Benalcazar, B. A. Bernevig, T. L. Hughes, Electric multipole moments, topological multipole moment pumping, and chiral hinge states in crystalline insulators. *Phys. Rev. B* **96**, 245115 (2017).
54. B. J. Wiede et al., Strong and fragile topological Dirac semimetals with higher-order Fermi arcs. *Nat. Commun.* **11**, 627 (2020).
55. K.-S. Lin et al., Spin-resolved topology and partial axion angles in three-dimensional insulators. *Nat. Commun.* **15**, 550 (2024).
56. M. Blanco de Paz et al., Tutorial: Computing topological invariants in 2d photonic crystals. *Adv. Quantum Technol.* **3**, 1900117 (2020).
57. M. B. de Paz, M. G. Vergniory, D. Bercioux, A. García-Etxarri, B. Bradlyn, Engineering fragile topology in photonic crystals: Topological quantum chemistry of light. *Phys. Rev. Res.* **1**, 032005 (2019).

Acknowledgments

Funding: The authors acknowledge funding from Singapore National Research Foundation Competitive Research Program grant NRF-CRP23-2019-0007 and Singapore Ministry of Education Academic Research Fund Tier 2 grant MOE-T2EP50123-0007. G.-G.L. acknowledge funding from Research Center for Industries of the Future (RCIF) at Westlake University grant No. 210000006022312 and Westlake Education Foundation grant No. 103110736022301. P.Z. acknowledges funding from National Natural Science Foundation of China grants No. 52022018, No. 52021001, No. 6101020101, and No. 62175215. Z.G. acknowledges the funding from the National Natural Science Foundation of China under grants No. 62375118, 62361166627, and 12104211, Guangdong Basic and Applied Basic Research Foundation under grant No.2024A1515012770, Shenzhen Science and Technology Innovation Commission under grants No. 20220815111105001 and 202308073000209, High level of special funds under grant No. G03034K004. Y.L. gratefully acknowledges the support of the Eric and Wendy Schmidt AI in Science Postdoctoral Fellowship, a Schmidt Futures programme. A.G.E., M.G.V., A.M.P, and C.D. acknowledge support from the Spanish Ministerio de Ciencia e Innovación grant PID2022-142008NB-I00. A.G.E., A.M.P., and C.D. acknowledge support from the Gipuzkoa Provincial Council within the QUAN-000021-01 project, as well as the Basque Government Elkartek program (KK-2023/00016). A.G.E. and M.G.V. acknowledge funding from the IKUR Strategy under the collaboration agreement between Ikerbasque Foundation and DIPC on behalf of the Department of Education of the Basque Government, Programa de ayudas de apoyo a los agentes de la Red Vasca de Ciencia, Tecnología e Innovación acreditados en la categoría de Centros de Investigación Básica y de Excelencia (Programa BERC) from the Departamento de Universidades e Investigación del Gobierno Vasco and Centros Severo Ochoa AEI/CEX2018-000867-S from the Spanish Ministerio de Ciencia e Innovación. M.G.V. thanks financial support from the Canada Excellence Research Chairs Program for Topological Quantum Matter, the Deutsche Forschungsgemeinschaft (DFG, German Research Foundation) GA 3314/1-1 – FOR 5249 (QUAST) and partial support from European Research Council (ERC) grant agreement No. 101020833. C.D. and A.M.P. acknowledge discussions with Inigo Robredo and Barry Bradlyn.

Author contributions: G.-G.L. and Q.W. initiated the project. S.M., Q.W., G.-G.L., C.D., A.M.-P., R.B., A.G.-E. and M.G.V. performed the theoretical explanation and developed the tight binding model simulations. G.-G.L. performed the simulation, designed the experiments, and analyzed the data. X.X., Z.W., Z.G. and G.-G.L. carried out the measurements. All authors discussed the results and contributed to the writing of the manuscript. B.Z. supervised the project. **Competing interests:** Authors declare no competing interests. **Data and materials availability:** All data are available in the manuscript, the supplementary material or deposited at DR-NTU (data) (*49*).

Supplementary Materials

Supplementary Text

Figs. S1 to S14

References (*50-57*)

Fig. 1. Schematic comparison between a 2D Chern insulator and a 3D axion insulator. (**A**) A Chern insulator characterized by a Chern number ($C = -1$) carries chiral edge states along its edges. (**B**) An axion insulator exhibits surface Chern insulator phases, with each surface characterized by a half Chern number ($C_s = \pm 1/2$). Chiral hinge states occur between two adjacent surfaces with contrasting surface Chern numbers. (**C**) When the 2D Chern insulator with $C = -1$ is attached to the top surface of the axion insulator with $C_s = +1/2$, the surface Chern number of the top surface changes to $C_s = -1/2$, thus redirecting the flow of chiral hinge states around the top surface.

Fig. 2. Construction of a photonic topological antiferromagnet. (**A**) Strategy for constructing a topological antiferromagnet. (**B**) Schematic of the tight-binding model that stacks 2D Haldane model layers with opposite magnetic fluxes in adjacent layers. (**C**) Design of the unit cell of the 3D photonic crystal. Each gyromagnetic rod (red or blue cylinder) is biased by an average external magnetic field of 0.18 T produced by a pair of permanent magnets (grey cylinders), with the magnetization direction represented by a white arrow. The lattice constant in the *x*-*y* plane is a = 16 mm. The periodicity along *z* is h = 14 mm. The dimensions are d = 4 mm, h_1 = 1 mm, h_2 = 1.5 mm, h_3 = 3 mm. Here, $b_1 = b_2$ = 10 mm. (**D**) Photograph of a fabricated experimental sample with 40 layers in the *z*-direction and 20×6 unit cells in the *x*-*y* plane. (**E**) Close-up view of the sample. The first two copper plates and one gyromagnetic rod layer on the top have been shifted for clarity. The coupling holes on the two adjacent copper plates have the same size. (**F**) Close-up view for one layer of gyromagnetic rods. The gyromagnetic rods and permanent magnets are embedded in dielectric foam to fix their positions. The permanent magnets are coated with high-conductivity materials. (**G**) Experimental setup for measurements of the surface states. (**H**) Measured surface dispersion on the A1 surface at different frequencies. Green lines indicate the simulated isofrequency contours. White dashed lines are guides to the eye that indicate the conical dispersion near the single surface Dirac point.

Fig. 3. Photonic axion insulator with chiral hinge states. (**A**) Unit cell of the photonic crystal. The parameters are the same as those in Fig. 2C except b_1 = 10 mm and b_2 = 5 mm. The coupling holes on the two adjacent copper plates have different sizes, thus breaking the mirror-reflection symmetry along the *z*-axis. (**B** and **C)** Measured field distributions excited by a point source at 11.9 GHz near the H1 hinge. A large copper plate with dimensions of 6 mm in the *z*-direction and 2×2 unit cells in the *x*-*y* plane is placed near the hinge as a metallic obstacle in (C). The sample has 40 layers in the *z*-direction and 20×6 unit cells in the *x*-*y* plane. The decay of electric fields results from the material losses. (**D**) Measured transmission spectra near the H1 hinge. The red solid line denotes backward transmission. The blue solid and dashed lines denote forward transmission without and with a metallic obstacle, respectively. The yellow rectangle indicates the simulated complete gap of the bulk and surface states from 11.65 to 12.24 GHz. (**E**) Measured hinge dispersion on the H1 hinge. The green curve and white region represent the simulated hinge states and projected bulk and surface states. (**F**) Illustration of the trajectory of chiral hinge states on a parallelogram-shaped photonic crystal with an odd number of photonic Chern insulator layers. Yellow and blue surfaces indicate surface Chern numbers of +1/2 and −1/2, respectively. (**G**) Measured field distribution in the sample shown in (F), excited by the point sources (red stars). The sample has 39 layers in the z-direction and 20×6 unit cells in the *x*-*y* plane. (**H** and **I**) Similar to (F and G) but with an even number of photonic Chern insulator layers. The sample has 40 layers in the *z*-direction and 20×6 unit cells in the *x*-*y* plane. (**J** to **M**) Similar to (F to I) but for a hexagonal prism structure. The hexagonal prism sample has 10 unit cells as the side width and 11 layers in the *z*-direction for panels (J and K), and 10 layers in the *z*-direction for panels (L and M), respectively. The colorscale of $|E_z|^2$ is linear.

Fig. 4. Braiding of chiral hinge states. (A and **D)** Illustration of the photonic crystal design with chiral hinge states performing a trefoil knot and a Hopf link, respectively. The design in (A) has 11 layers in the *z*-direction, and its length in *x* direction consists of 32 unit cells. The design in (D) is formed by merging two parallelogram-shaped prisms, each with 15 layers in the *z* direction and dimensions in *x*-*y* plane of 10×6 unit cells. (**B** and **E**) Corresponding measured field distributions of chiral hinge states illustrated in (A and D), respectively. (**C** and **F**) Corresponding topology diagrams. The colorscale of $|E_z|^2$ is linear.

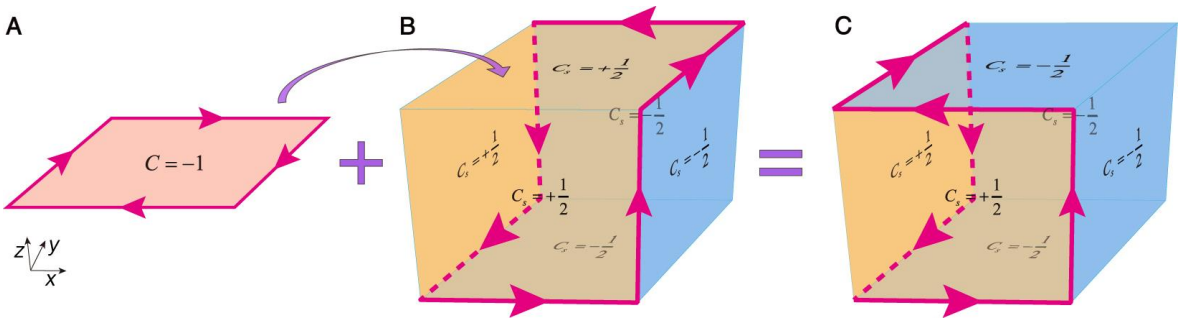

418
419

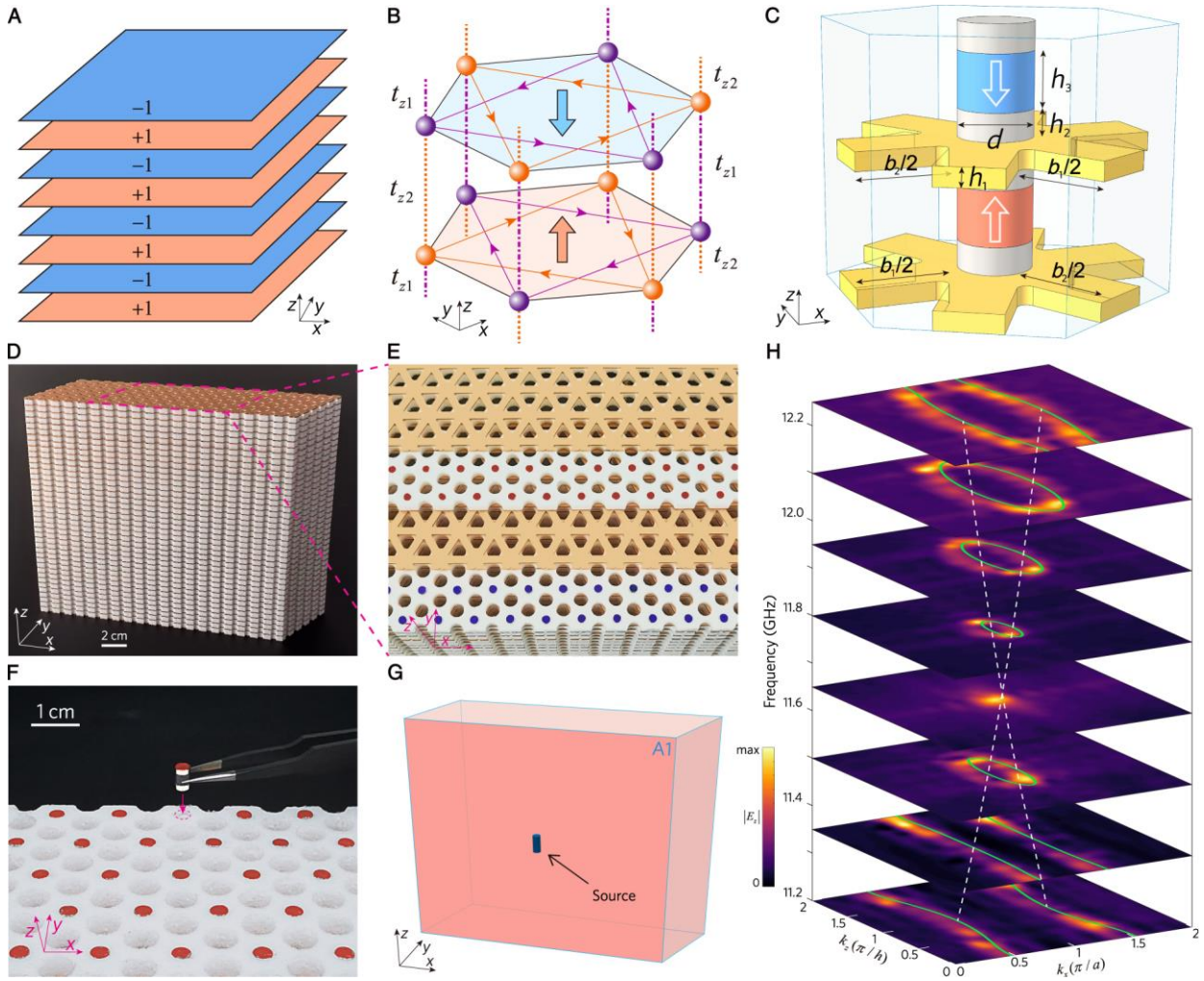
A
−1
+1
−1
+1
−1
+1
−1
+1
B
t_{z1}
t_{z2}
C
h_3
h_2
h_1
d
$b_2/2$
$b_1/2$
D
2 cm
E
F
1 cm
G
A1
Source
H
Frequency (GHz)
12.2
12.0
11.8
11.6
11.4
11.2
max
0
$|E_z|$
$k_z(\pi/h)$
$k_x(\pi/a)$

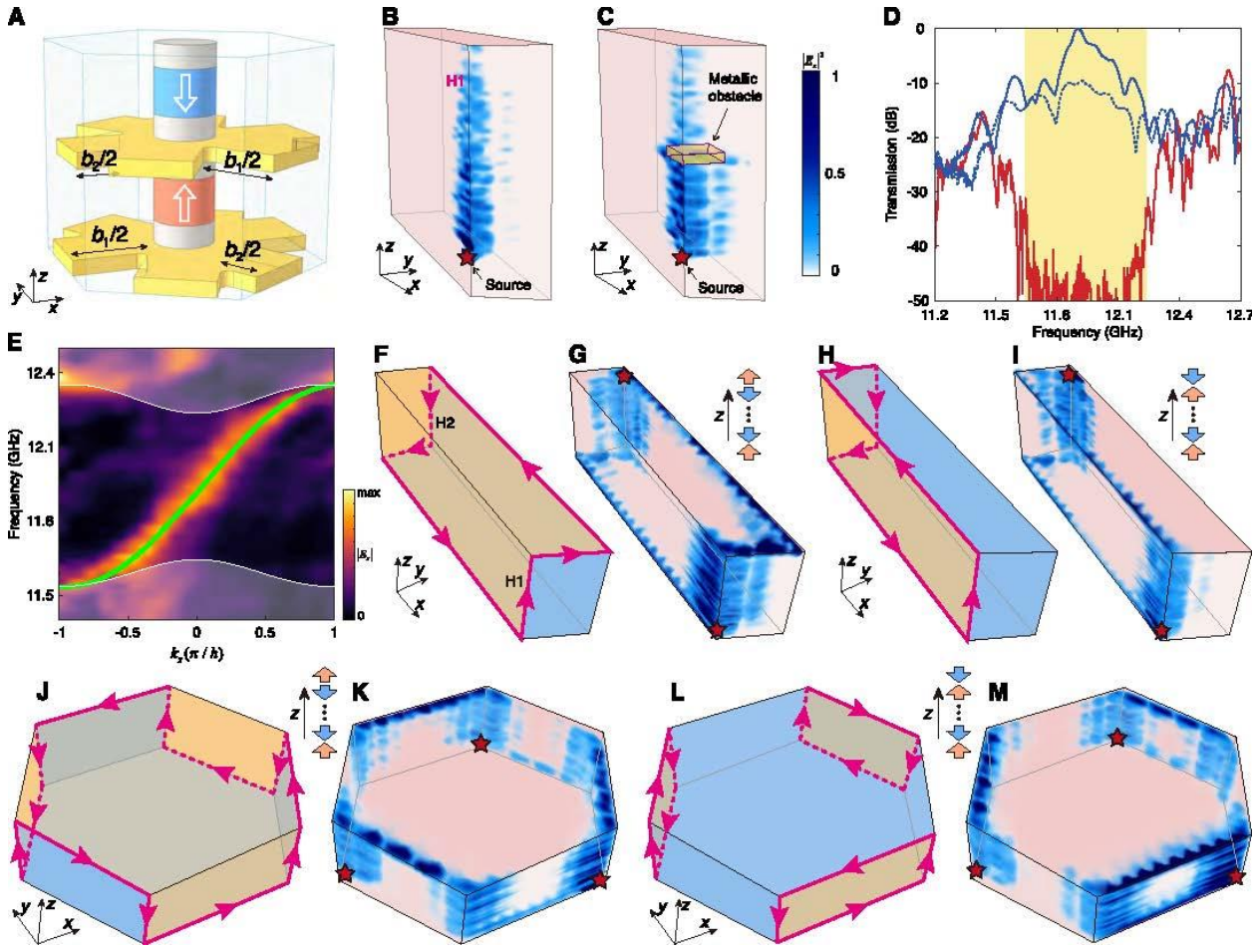
A
B
C
D
H1
Source
Metallic obstacle
Transmission (dB)
Frequency (GHz)
E
F
G
H
I
H2
H1
Frequency (GHz)
J
K
L
M

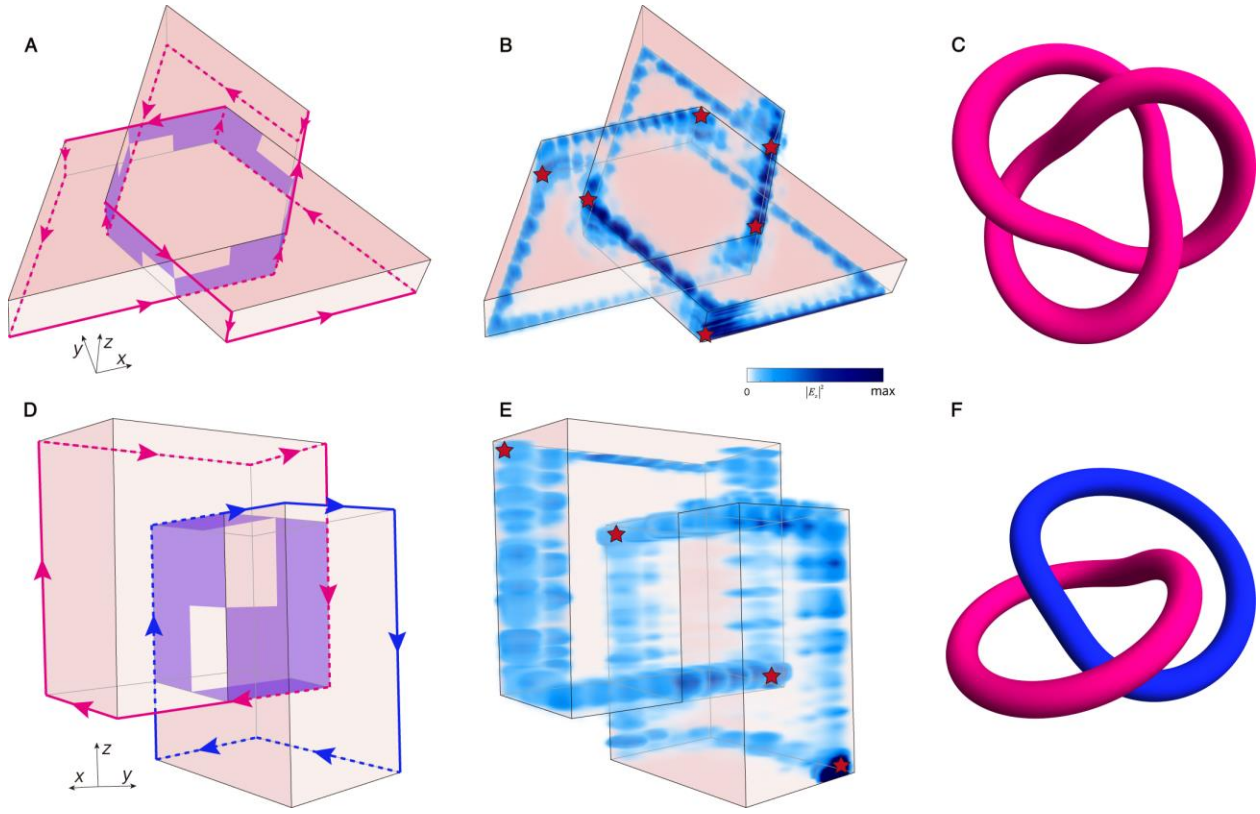

425